Title

Carbon—Mineral Slurry Electrodes for Energy-Efficient Lithium Leaching from Low-Grade Clay Feedstocks

Journal

Environmental Science and Technology, 60(8)

ISSN

0013-936X

Authors

Haddad, Andrew Z
Cha, Hyungyeon
Adibnia, Sahand
et al.

Publication Date

2026-03-03

DOI

10.1021/acs.est.5c11515

Environmental Science & Technology

pubs.acs.org/est

Article

Carbon–Mineral Slurry Electrodes for Energy-Efficient Lithium Leaching from Low-Grade Clay Feedstocks

Andrew Z. Haddad,* Hyungyeon Cha, Sahand Adibnia, Xander B. Fleming, Liam McDonough, Floria Li, Siva Bandaru, Raynald Giovine, Chaochao Dun, Garrett Pohlman, Lukas Hackl, Bilen Akuzum, Jeffrey J. Urban, and Robert Kostecki*

Cite This: *Environ. Sci. Technol.* 2026, 60, 6162–6176

Read Online

ACCESS | Metrics & More | Article Recommendations | Supporting Information

ABSTRACT: Lithium extraction from clay deposits is typically hampered by low lithium grades and the high capital and energy demands of conventional processing. We report an ambient temperature electrochemical leaching method that bypasses high-temperature roasting and concentrated-acid leaching, directly liberating 93% of lithium from low-grade hectorite in 24 h at 1 V, with 77% Faradaic efficiency, an energy intensity of 3.91 MWh/t lithium carbonate equivalent (LCE). Utilizing a carbon–mineral composite slurry electrode strategy we achieve electron-driven lattice deconstruction through iron oxidation coupled with proton uptake to drive lithium deintercalation, offering a new strategy for low-temperature critical-metal recovery. A preliminary cost analysis highlights pathways to achieving cost intensities below $3000/t LCE. Challenges remain in improving current density, extraction kinetics, and demonstrating process scalability, however, this work establishes a foundation for effective electrochemical lithium extraction from abundant but previously uneconomical clay deposits.

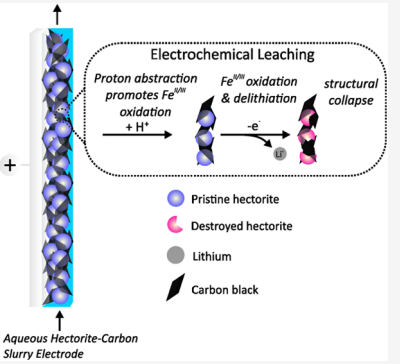

KEYWORDS: *critical materials and minerals, lithium extraction, conductive composites, slurry electrodes, mineral composites*

INTRODUCTION

The demand for lithium is rapidly increasing due to its critical role in lithium-ion batteries for electric vehicles and grid-scale energy storage. By 2025, annual lithium demand is projected to reach 85,000 t, representing a 300% increase from 2018 levels, and could grow to 413,000–704,000 t per year by 2100.[1−6] Despite an estimated 86 million metric tons of total lithium resources,[7] economic and environmental challenges in extraction and refinement remain major barriers to scaling supply.

Lithium is primarily sourced from brines and hard rock minerals such as spodumene. Brine-based extraction, predominantly in South America's Lithium Triangle, relies on solar evaporation, a cost-effective but slow process to produce lithium carbonate.[8−10] In response, direct lithium extraction (DLE) technologies have emerged, particularly for geothermal sources.[11,12] However, DLE remains largely at the pilot stage, with only one commercial-scale operation in Argentina (Salar del Hombre Muerto Western Subbasin).[11] Meanwhile, spodumene processing continues to dominate lithium supply, accounting for 52–55% of global production.[4,8,11,13] Conventional spodumene processing involves high-temperature roasting (~1100 °C) followed by acid leaching,[14] leading to high energy consumption and carbon emissions.

Clay-hosted lithium deposits, such as those found in the McDermitt Caldera (USA), southern Nevada, Mexico, California, China, and Serbia, are an attractive alternative due to their abundance and widespread geographic distribution.[15−18] However, low lithium grades, typically 0.1–0.31 wt % Li, and energy-intensive extraction processes have hindered commercial viability. Conventional methods include sulfate roasting at ~950 °C and direct sulfuric acid leaching, both of which incur high capital and operational costs.[19−28] Additionally, these methods are highly carbon-intensive, emitting up to 22 tons of CO_2 per ton of lithium produced, more than twice the emissions of steel production.[6,22,29] These cost, energy, and environmental impacts, combined with the historical economic inequality of lithium-rich regions, underscore the need for more energy-efficient extraction technologies.

Electrochemical leaching presents a promising alternative by leveraging electrical energy to extract lithium without high temperatures or concentrated acids and can be powered by renewable energy.[30,31] It has been successfully applied in electronic waste remediation,[30,32−34] lithium-ion battery recycling,[31,35,36] and ore dissolution.[37−39] However, despite the conceptual appeal of electrochemical leaching, its

Received: September 10, 2025
Revised: February 3, 2026
Accepted: February 4, 2026
Published: February 18, 2026

https://doi.org/10.1021/acs.est.5c11515
Environ. Sci. Technol. 2026, 60, 6162–6176

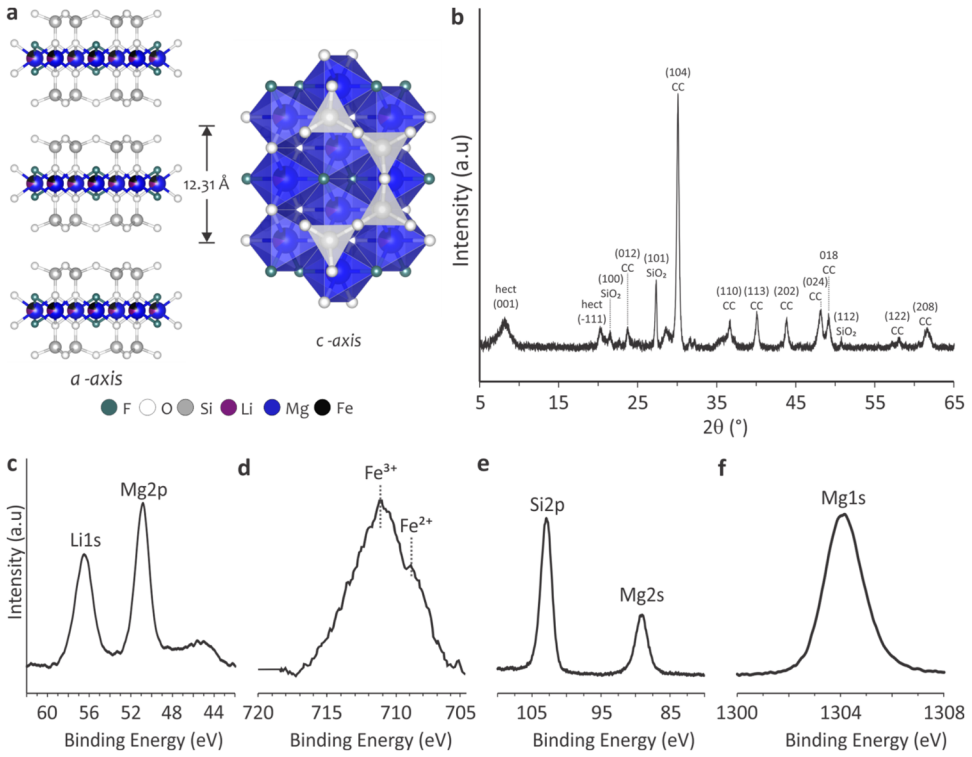

Figure 1. Structure, crystallographic, and spectroscopic characterization of hectorite. (a) *a*-Axis and *c*-axis views of the crystal structure of hectorite showing 2D stacking of the 2:1 sheet. (b) X-ray diffraction pattern of pristine hectorite (black) showing main hectorite diffraction plane at 7° 2θ as well as crystalline planes of calcium carbonate (CC) and quartz (SiO_2) admixtures. (c) High resolution Li 1s XPS spectrum of pristine hectorite (black). (d) High resolution Fe 2p spectrum of pristine hectorite (black). (e) High resolution Si 2p spectrum of pristine hectorite (black). (f) High resolution Mg 1s spectrum of pristine hectorite (black).

application to oxide- and silicate-based ores remains limited by several fundamental challenges. Foremost, is the intrinsically insulating nature of most clay minerals,[40] which restricts electronic percolation and limits the extent of redox-driven lattice breakdown. Second, there are the large overpotentials and sluggish kinetics arising from poor electron and ion transport within the mineral matrix, and third, low Faradaic efficiency in aqueous environments where parasitic proton reduction can compete with productive metal oxidation. These constraints have hindered the development of practical, low-voltage electrochemical routes capable of achieving high lithium, or other metal ion, extraction from sedimentary clays and oxide ores.

Several strategies to enhance electron transfer kinetics have been studied including using soluble chemical promoters to initiate reactions before ion migration,[38] applying acoustic waves,[41,42] or utilizing conductive molten salt electrolytes.[43−45] Recently, we reported a new method for electrochemical lithium-ion dissolution from hectorite ores, achieving direct electrochemical activation.[46] The approach involves mixing conductive additives (e.g., carbon black) with the ore to form carbon-mineral composites, enabling enhanced electronic percolation. Our prior work, which investigated the mechanism of lithium deintercalation during the anodic polarization of hectorite-carbon black composite electrodes (HCCEs), found that electrochemical activation promoted lithium-ion release and a complete structural breakdown of the lattice via iron oxidation and lithium deintercalation. That work provided a solid-state proof-of-concept of electrochemical activation, operated in organic electrolyte at high anodic potentials (3.4−4.5 V vs Li/Li^+), and achieved partial ion release within a positive-electrode environment. Encouraged by those results we sought to validate electrochemical leaching in an industrial-relevant aqueous leaching environment which mimic hydrometallurgical leaching conditions. Key process design criteria included: (i) abundant, inexpensive materials for the anode and cathode; (ii) membrane-free operation to reduce complexity; (iii) optimized carbon black loading for maximum reaction rates; (iv) a dilute acidic electrolyte to minimize acid use; (v) high Faradaic efficiency; and (vi) low energy intensity.

In this study, using a 90−10 hectorite-carbon black aqueous composite slurry electrode (HCSE) 93% lithium is removed from hectorite in 24 h, through an iron-redox/proton-coupled dissolution mechanism that governs clay decomposition, affording a Faradaic efficiency of 77%, and an energy intensity of 3.91 MWh/t lithium carbonate equivalent (LCE) at 1 V. Our conclusions are supported by a mechanistic study, an evaluation of conductive additive effects, applied potential optimization, and a structural post-mortem analysis of the leachate residue. A preliminary operational cost and energy assessment benchmarks our method against existing and emerging electrochemical leaching technologies, and sensitivity analysis identifies the main drivers of total cost and energy consumption, contextualizing our results and highlighting key areas for future improvement. The findings establish electrochemical leaching as an energy-, and potentially cost-effective, alternative for lithium recovery from abundant low lithium grade clay deposits.

https://doi.org/10.1021/acs.est.5c11515
Environ. Sci. Technol. 2026, 60, 6162−6176

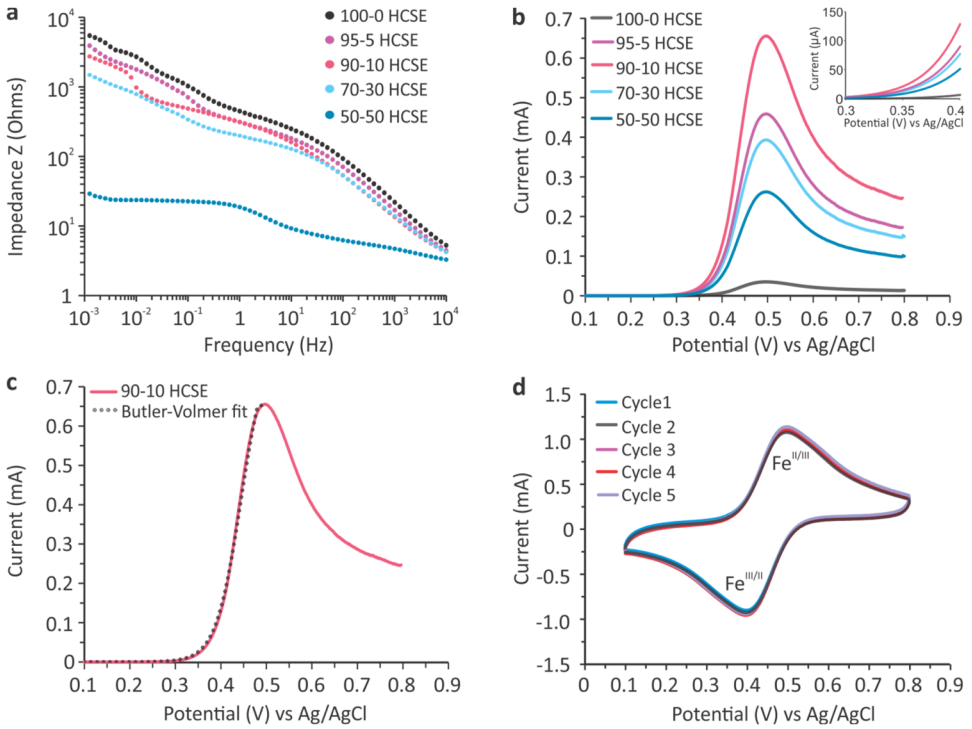

Figure 2. Electrochemical characterization of HCSEs. (a) Bode plots of HCSEs with hectorite to carbon black ratios of 100−0 (black), 95−5 (purple), 90−10 (red), 70−30 (light blue), and 50−50 (dark blue). (b) LSVs of HCSEs with hectorite to carbon black ratios of 100−0 (black), 95−5 (purple), 90−10 (red), 70−30 (light blue), and 50−50 (dark blue). (c) Fit of LSV of 90−10 HCSE (red) to the Butler−Volmer equation (black dotted). (d) CV of 90−10 HCSE cycled five times. All experiments were performed in triplicate.

RESULTS AND DISCUSSION

Structure, Morphology, Surface Chemistry of Hectorite

Hectorite, a smectite clay, consists of an octahedral layer of Mg^{2+}, Fe^{2+}, or Li^{+} ions coordinated by oxygen or fluoride atoms, sandwiched between two layers of linked SiO_4 tetrahedrons. These sheets stack in a turbostratic structure, interconnected by cations (Na^{+}, K^{+}, Ca^{2+}) and water molecules, Figure 1a.[47−55] The hectorite used in this study was sourced from the Rio Tinto US Borax mine in Boron, California, where it is classified as a gangue byproduct of boron refining. This makes it a compositionally complex material containing various mineral admixtures, including hectorite, silica, borates, alumina, and calcium carbonate. Inductively coupled plasma mass spectrometry (ICP-MS) analysis, Table S1, confirmed high fractions of B_2O_3 (12.8 wt %) and SiO_2 (62.87 wt %), with notable Al_2O_3 (4.65 wt %) and CaO (3.20 wt %). The remaining material includes expected hectorite constituents, magnesium, iron, sodium, lithium, and potassium, yielding a lithium grade of 0.5 wt % Li_2O, within the typical range for sedimentary clays.[19] X-ray diffraction (XRD) patterns, Figure 1b, show dominant peaks for calcium carbonate and silica, along with the characteristic monoclinic hectorite 001 reflection at 7° 2θ, corresponding to interplanar spacing in hectorite's silicon layers.[15,56]

X-ray photoelectron spectroscopy (XPS) and ICP-MS were used to analyze the valence states and elemental composition of hectorite. ICP-MS revealed that the three octahedral cations, Li, Fe, and Mg, have a stoichiometric ratio of ∼1:10:14 when normalized to Li, consistent with XPS surveys, Figure S1. This composition aligns with previous studies of monoclinic trioctahedral hectorite, yielding the structural formula $(Li_{0.12}Fe_{1.2}\ Mg_{1.68})Si_4O_{10}(OH,F)_2$.[57] Our prior work on HCCEs characterized metal valencies using depth-penetrating XPS and electron energy-loss spectroscopy (EELS).[46] XPS analysis showed a Li 1s core level at 56.6 eV, confirming lithium as a primary octahedral cation in trioctahedral smectites.[47] Iron exhibited mixed valency, with Fe^{2+} (42%) and Fe^{3+} (58%) corresponding to core levels at ∼708 eV and ∼ 711 eV, respectively. High-resolution XPS of the HCSEs were consistent with our previous analysis of the HCCEs, showing Li 1s at 56.6 eV, Figure 1c, and mixed iron valency, Figure 1d. Additional spectra of Si 2p and Mg 1s confirmed oxidation states of Si^{4+} and Mg^{2+}, with core levels at ∼103 eV and ∼89 eV, respectively, Figure 1e,f.

These structural and compositional features are directly related to the challenge of lithium recovery from hectorite. Lithium resides primarily in octahedral sites within a robust trioctahedral sheet coordinated by Mg^{2+} and Fe^{2+}/Fe^{3+}, all encapsulated between SiO_4 tetrahedral layers that confer substantial lattice stability. The interlayer region containing Na^{+}, K^{+}, and Ca^{2+}, are readily exchangeable, but the octahedral Li^{+} is strongly bound and not easily liberated by mild acid leaching. This intrinsic structural rigidity, combined with the mineral's electrical insulating nature, creates kinetic and thermodynamic barriers that limit the extent of lithium removal in conventional hydrometallurgical processes. Electrochemical activation directly targets these constraints. Oxidation of Fe^{2+} within the octahedral sheet perturbs local charge balance and weakens metal−oxygen coordination, while proton uptake facilitates partial dehydroxylation and destabilization of Mg−O and Fe−O bonding environments. Such redox-coupled chemical processes initiate a progressive lattice deconstruction that releases Li^{+} into the aqueous phase. Introducing carbon black into the composite further enables this mechanism by providing the electronic percolation

https://doi.org/10.1021/acs.est.5c11515
Environ. Sci. Technol. 2026, 60, 6162−6176

necessary for charge propagation through the insulating mineral matrix.

Effect of Conductive Additive and Acid Concentration on Electrochemical Leaching

As discussed, electrochemical leaching is often limited by poor electron transfer in insulating materials. The hectorite ore used here faces this challenge, where high resistance impedes electron movement and percolation. Consequently, the efficiency of electron transport in HCSEs influences the limiting current and reaction rate. To examine this, we investigated the electrical conductivity and impedance of HCSEs with varying carbon black content using both direct current (DC) and alternating current (AC) methods.

Hectorite and carbon black were ball-milled for 15 min to produce the composite powders with ratios of 100−0, 95−5, 90−10, 70−30, and 50−50. XRD analysis confirmed that ball-milling did not alter the hectorite lattice, as diffraction patterns remained unchanged, Figure S2. The milled composite powders were then immersed in 0.125 M H_2SO_4 electrolyte to form the HCSEs. Electrochemical impedance spectroscopy (EIS) was performed from 10^4 to 10^{-3} Hz with a 50 mV AC voltage. Bode impedance plots identified key frequency transitions from interfacial impedance to bulk conductivity and from bulk conductivity to bulk capacitance.[58] As shown in Figure 2a, carbon black content substantially influenced impedance. HCSEs with 100−0, 95−5, 70−30, and 50−50 compositions exhibited a transition from interfacial impedance to bulk conductivity around 10^{-1} Hz, followed by a shift to bulk capacitance near 10^{1} Hz. In contrast, the 90−10 HCSE transitioned to bulk conductivity at a lower frequency, ∼10^{-2} Hz, while maintaining the same bulk capacitance transition. Direct current (DC) conductivity measurements, Figure S3, followed a similar trend, increasing from 171 μS/cm (100−0 HCSE) to 8221 μS/cm (50−50 HCSE). Notably, adding just 5 and 10 wt % carbon black led to 34% and 75% increases in conductivity, respectively, suggesting that minimal carbon black additions considerably enhance electron transport. While increased carbon content improves bulk conductivity, the enhanced activity of the 90−10 HCSE cannot be attributed to percolation alone. The 90−10 composition represents a balance between forming a continuous conductive network and maintaining a high density of electrochemically accessible hectorite. At lower carbon contents (100−0, 95−5), electronic percolation is incomplete, leaving large regions of each particle electrically isolated and limiting both current and extent of reaction. Conversely, at higher carbon loadings (70−30, 50−50), the hectorite fraction becomes increasingly diluted and carbon-rich agglomerates form, reducing the uniformity of carbon coating on mineral grains and decreasing the effective interfacial area between the conductive additive and the active clay. These morphological effects hinder electron transfer into the particle interior despite higher bulk conductivity. The 90−10 ratio therefore sits near an optimal point where carbon forms a continuous but not overly clustered network, maximizing particle-level active-material coverage, electron-accessible surface area, and reaction-zone density. This explains why the 90−10 HCSE displays the highest current response and rate constant, despite higher-carbon slurries exhibiting greater intrinsic conductivity.

Beyond improving bulk conductivity, carbon black also impacts the extent of reaction at the level of individual mineral particles. Pure hectorite (100:0) is highly insulating, so electron transfer into the particle interior is limited to a thin shellnear the electrode interface. As a result, only surface regions undergo Fe^{2+} oxidation and lithium deintercalation, while the particle cores remain electronically isolated. In 90:10 HCSEs, carbon establishes a percolating conductive network that distributes electronic pathways across and between mineral grains, increasing the electrochemically addressable surface area and enabling a greater fraction of each particle to undergo redox-driven lattice deconstruction. This mechanism is consistent with the pronounced increase in current and charge passed between 100:0 and 90:10 compositions. A more detailed microstructural and electronic analysis of the ball-milled composite, such as tracking particle−contact evolution, modeling electronic percolation behavior, or probing interfacial electronic structure, would provide deeper insight into the origins of conductivity enhancement. Future investigations employing advanced imaging and modeling techniques will be essential for further optimizing composite design and improving electron-transfer efficiency in slurry-based systems.

Linear sweep voltammetry (LSV) was conducted to evaluate current response in HCSEs. The setup included an acid-resistant mixed metal oxide (Ti/Ta/Ir) anode, a platinum wire cathode, and an Ag/AgCl reference electrode. A 100 g/L suspension of active material in 0.125 M H_2SO_4 was homogenized before data collection. LSV curves, recorded at 0.5 mV/s, showed a pronounced oxidation event peaking at 0.5 V vs Ag/AgCl, Figure 2b. The 90−10 HCSE exhibited the highest current response, ∼0.7 mA, indicating iron oxidation and lithium leaching, consistent with our previous immobilized HCCE study.[46] LSVs in pure 0.125 M H_2SO_4 showed no current response at 0.5 V, Figure S4. HCSE composition influenced the observed onset potential for oxidative current, which we define as the potential at which measurable anodic current associated with Fe^{2+} oxidation and lithium deintercalation begins, Figure 2b inset. Because this onset reflects kinetic, transport, and interfacial effects in the slurry electrode, it should not be interpreted as the thermodynamic standard potential or formal potential of the hectorite redox couple. Rather, the onset potential serves as a practical indicator of when the redox-driven lattice-deconstruction pathway becomes active under our experimental conditions, but it does not represent the intrinsic E^0 or $E^{0\prime}$ of the Fe^{2+}/Fe^{3+} couple in hectorite. Interestingly, current response trends did not align with impedance and conductivity trends, suggesting excess carbon black may hinder reaction kinetics. Additionally, the leaching potential is well below water oxidation, observed at 1.2 V vs Ag/AgCl, indicating that the process could benefit from high Faradaic efficiency and low energy consumption.

To determine the standard rate constant (k^0) for the oxidative leaching reaction, we modeled the current−potential curves using the Butler−Volmer equation.[59] We fit our LSV data to the classic Butler−Volmer model of electrode kinetics.[59,60] For a one-step, one-electron oxidation reaction, the oxidative current (i_{BV}) is defined by eq 1

$$i_{BV} = \frac{i_d}{1 + e^{-(F(E-E^0)/RT) + K_0^{-1} e^{-\left(F(1-\alpha)(E-E^0)/RT\right)}}} \quad (1)$$

where i_d is the diffusion-limited current, F is the Faraday constant, R is the molar gas constant, T is temperature (K), E is the applied potential, E^0 is the formal potential of the redox-couple, α is the transfer coefficient, and K_0 is the dimensionless heterogeneous rate constant,[60] $K_0 = FAC k^0/i_d$, where A is the

https://doi.org/10.1021/acs.est.5c11515
Environ. Sci. Technol. 2026, 60, 6162−6176

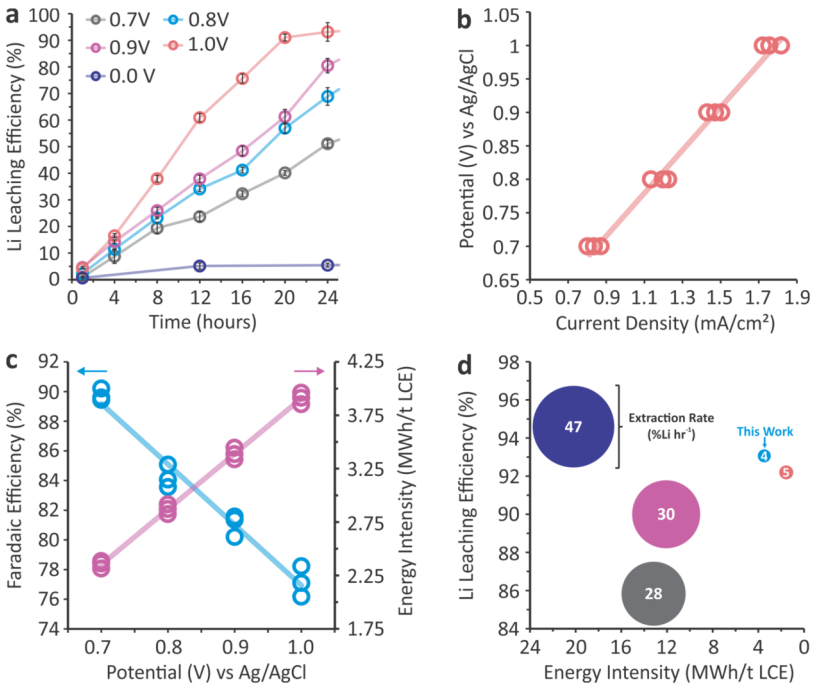

Figure 3. Performance and energy metrics of electrochemical leaching. (a) Electrochemical lithium leaching efficiency vs test time for applied potentials of 0.7 (black), 0.8 (blue), 0.9 (purple), and 1.0 (red), and 0.0 (gray) volts. (b) Mean current density with respect to applied potential during electrochemical leaching. (c) Faradaic efficiency (blue) and energy intensity (purple) as a function of applied potential. (d) Plot of energy intensity vs Li extraction efficiency for industrial spodumene leaching (dark blue), industrial clay sulfate roasting (purple), industrial clay sulfuric acid leaching (gray), electrochemical spodumene leaching (red), and electrochemical clay leaching (this work) (light blue). Bubble size represents the lithium extraction rate (% Li removed per hour) of each process.

electrode surface area, C is the bulk concentration of the electroactive species, and k^0 is the standard heterogeneous rate constant. While we use the onset potential operationally, the formal potential of the redox process could, in principle, be extracted by fitting quasi-reversible voltammograms using peak-fitting or kinetic-modeling tools when the electron-transfer step is well-defined. In our system, the redox event is coupled to proton transfer and solid-state structural change, making the extraction of a single formal potential nontrivial. Therefore, we restrict our analysis to kinetic fits of the observable voltammetric response.

Nonlinear least-squares fitting of experimental voltammograms for each HCSE composition was performed using the Levenberg–Marquardt algorithm, with k^0, α, and i_d as fitting parameters. E^0, C and A were fixed for each LSV curve: E^0 was set to the onset potential from each LSV, $C = 7.5 \times 10^{-5}$ mol/cm^3, and $A = 2.1545$ cm^2, representing the electrode's geometric area. Fitting data for all HCSE compositions is provided in Figure S5, with Figure 2c showing the results for the 90–10 HCSE. The calculated rate constants, Figure S6, indicate that carbon black content slightly influences k^0 due to variations in E^0 across LSV curves. The highest rate constant, 1.21×10^{-6} cm/s, was observed for the 90–10 HCSE, while the 100–0 HCSE (no carbon black) had a lower k^0 of 7.55×10^{-7} cm/s. Excessive carbon black appears to hinder uniform active material coating and electron percolation, a phenomenon also observed in lithium-ion batteries.[61] Figure 2d displays cyclic voltammograms (CV) over five cycles, confirming a reversible oxidation–reduction process and demonstrating high electrochemical activity within the studied potential range. To assess the role of protons in the reaction mechanism, LSV curves were collected for the 90–10 HCSE in increasing H_2SO_4 concentrations (0.025–0.2 M, in 0.025 M increments). As shown in Figure S7a, no anodic current was observed below 0.075 M, after which it increased with acid concentration in a first-order dependence, Figure S7b. This trend aligns with the Pourbaix diagram of iron,[62] indicating that acidic conditions promote Fe^{2+}/Fe^{3+} oxidation, facilitating lithium oxidative deintercalation from hectorite.

Our prior ICP-MS and XPS analysis revealed that Fe^{2+} is more abundant than Li in hectorite, with 0.83 μmol of Fe^{2+} available for oxidation under the conditions used in our CV and LSV experiments. This raised the question of whether all Fe^{2+} is oxidized or only the fraction necessary for lithium deintercalation. Integration of the anodic charge under the CV curve yielded a total charge of 78.6 mC, closely matching the theoretical charge of 80.2 mC for complete oxidation of 0.83 μmol Fe^{2+} indicating that nearly all iron is oxidized during the leaching process. Since electrochemical reactions must conserve charge and given that lithium is less abundant than Fe^{2+}, this implies that the reaction is coupled with proton transfer, compensating for net charge through chemical interactions with other metal oxides in hectorite. The dissolution of magnesium and iron oxides in sulfuric acid is known to be exergonic,[20] and previous studies showing that magnesium octahedra are preferentially attacked in acidic H_2SO_4 media.[63,64] To further clarify the reaction mechanism, we constructed a thermodynamic square, Figure S8, starting from neutralized hectorite as shown in reaction 2.

$$2[(Li_{0.12}Fe^{II}_{0.5}Fe^{III}_{0.7}Mg_{1.68})Si_4O_{10}(OH, F)_2]^{2-} + 4H^+ \rightarrow [(Li_{0.12}Fe^{II}_{0.5}Fe^{III}_{0.7}Mg_{1.68})Si_4O_{10}F_2] + 4H_2O \quad (2)$$

https://doi.org/10.1021/acs.est.5c11515
Environ. Sci. Technol. 2026, 60, 6162–6176

Since no anodic current was observed without acid, we rule out initial oxidation as the first step and instead identify protonation as the initial reaction step. This is followed by the electrochemical oxidation of iron, forming a protonated and oxidized dication intermediate, Figure S8, which then transitions to a neutral species through the release of both lithium and magnesium, as represented by anodic reaction 3.

$$2[(Li_{0.12}Fe^{II}_{0.5}Fe^{III}_{0.7}Mg_{1.68})Si_4O_{10}F_2] + H^+ \rightarrow 2[(Fe^{III}_{1.2}Mg_{1.24})Si_4O_{9.5}F_2] + 0.24Li^+ + 0.88Mg^{2+} + 0.5H_2O + +1e^- \quad (3)$$

The cathodic reaction is the reduction of protons to hydrogen gas, given by the cathodic reaction 4.

$$1H^+ + 1e^- \rightarrow 0.5H_2 \quad (4)$$

The net reaction describes a process in which iron protonation and oxidation initiate leaching, leading to lithium deintercalation and magnesium dissolution via acidic proton attack to maintain charge balance, as shown in reaction 5, which establishes the electrochemical conditions under which the redox-driven lattice-deconstruction mechanism emerges, providing the basis for mechanistic interpretation.

$$2[(Li_{0.12}Fe^{II}_{0.5}Fe^{III}_{0.7}Mg_{1.68})Si_4O_{10}F_2] + 2H^+ \rightarrow 2[(Fe^{III}_{1.2}Mg_{1.24})Si_4O_{9.5}F_2] + 0.24Li^+ + 0.88Mg^{2+} + 0.5H_2 + 0.5H_2O \quad (5)$$

Effect of Operating Conditions on Electrochemical Leaching

To assess leaching efficiency, kinetics, and Faradaic efficiency, potentiostatic leaching was performed at 0.7, 0.8, 0.9, and 1.0 V, with 0.0 V serving as an acid leach control. Batch tests used 100 g/L of the 90−10 composite in 0.025 L of 0.125 M H_2SO_4. A mixed metal oxide (Ti/Ta/Ir) anode (2.15 cm^2 active area), platinum wire cathode, and Ag/AgCl reference electrode were used, Figure S9. To determine feasible clay loadings, we measured the viscosity of the 90−10 HCSE at 25, 50, 100, and 150 g/L. As shown in Figure S10a, viscosity increased gradually from 25 to 100 g/L but rose sharply at 150 g/L, informing our choice of 100 g/L loadings. Stress vs shear rate plots, Figure S10b, confirmed Newtonian behavior of the HCSEs.

Figure 3a shows the effect of applied potential on lithium extraction. At 1.0 V, 93.13% ± 3.52% of lithium was leached within 24 h, with extraction decreasing with lower potentials. The 0.0 V control achieved only 5.44% ± 0.74%, consistent with previous reports on room-temperature acid leaching of hectorite.[63] Figure 3b illustrates reaction kinetics, showing a linear decrease in current density with decreasing potential. The observed current density range (0.84−1.77 mA/cm^2) is order of magnitude lower than industrial electrowinning processes. Contextualizing our current densities is difficult due to the lack of similar studies that operate at low voltage and low current density, but they are comparable to other few reported low voltage electrochemical leaching studies. Jang et al. reported 0.2−0.5 mA/cm^2 at 1−1.4 V for lithium recovery from LIBs,[36] and Lee et al. observed 3.2−32.2 mA/cm^2, dependent on voltage, for nickel leaching from laterite ores, while Makarova et al. reported 10−20 mA/cm^2 for rare earth element leaching from spent NdFeB magnets at 8−20 V.[34] Each study noted that higher extraction rates correlated with higher current densities but also led to sharp power increases and reduced Faradaic efficiencies, aligning with our observations

Figure 3c shows the effect of potential on Faradaic efficiency and energy intensity. The Faradaic efficiency peaks at 89.75% ± 0.3 at 0.7 V, and decreases to 77.20% ± 0.8 at 1.0 V, see Figure S11 for calculation details. Because hectorite's oxidation potential is well below the water oxidation reaction (WOR), electrochemical leaching achieves both high lithium extraction (∼93%) and Faradaic efficiencies (77−89%). However, the process remains slow, requiring long leach times, consistent with the low current densities. Energy intensity peaks at 3.9 MWh/t LCE at 1.0 V and has a low of 2.35 MWh/t LCE at 0.7 V, demonstrating the compromise between either lower energy consumption or higher extraction efficiency. Collectively, the performance metric results highlight an advantage of electrochemical leaching. Unlike other electrochemical methods that rely on acid alone[30] or a combination of acid and chemical oxidants,[38] our approach leverages the transition metal redox chemistry to break down the lattice and release lithium, which offers tunability to favor either higher extraction rates or lower energy intensity.

Table S2 presents lithium concentrations over time for all leaching experiments, while Table S3 provides the full IC characterization of the leachate. Other monovalent alkaline ions, such as sodium and potassium, exhibited high leaching efficiencies of 94.08% and 94.44%, respectively, as expected due to their labile positions in between the 2:1 clay sheets. Divalent calcium and magnesium had lower leaching efficiencies of 31.25% and 22.45%, respectively, with magnesium removal agreeing well with the predicted 27% based on reaction 5. To contextualize these results, we compared lithium extraction at 1.0 V with industrially used clay leaching methods, direct sulfuric acid leaching and sulfate roasting,[22,26] the commercial process for lithium extraction from spodumene,[28] and a recently reported electrochemical spodumene leaching method,[38] Figure 3d. Our electrochemical process outperforms all other clay leaching technologies, achieving higher extraction efficiency with lower energy intensity. However, when comparing against all feedstocks, the process has a higher energy intensity than electrochemical spodumene leaching (1.58 MWh/t LCE), due to spodumene's ∼17 times higher lithium content than the clays used in this study.[38] Electrochemical leaching delivers a higher total lithium recovery than today's best conventional clay leaching methods, but it proceeds slowly, removing only 3.8% of the lithium per hour. By comparison, industrial leaching processes, such as sulfuric-acid leaching and sulfate roasting for clays, remove lithium far faster, about 28%[26] and 30%[22] per hour, respectively, while traditional spodumene leaching achieves approximately 47% per hour.[65] Still, our rate is consistent with other electrochemical techniques; for example, electrochemical spodumene leaching reports ∼4.6% Li removal per hour,[38] Figure 3d.

Given that some industrial clay leaching processes rely heavily on acid, we also assessed acid consumption in our electrochemical leaching method. At the Thacker Pass facility,[26] sulfuric acid leaching at 90 °C requires 0.49 t of concentrated H_2SO_4 per t of clay. By contrast, our process reduces acid use by 70%, requiring only 0.147 t H_2SO_4 per t of clay, while operating at room temperature. This is significant, as sulfuric acid costs, driven by liquid sulfur consumption,

https://doi.org/10.1021/acs.est.5c11515
Environ. Sci. Technol. 2026, 60, 6162−6176

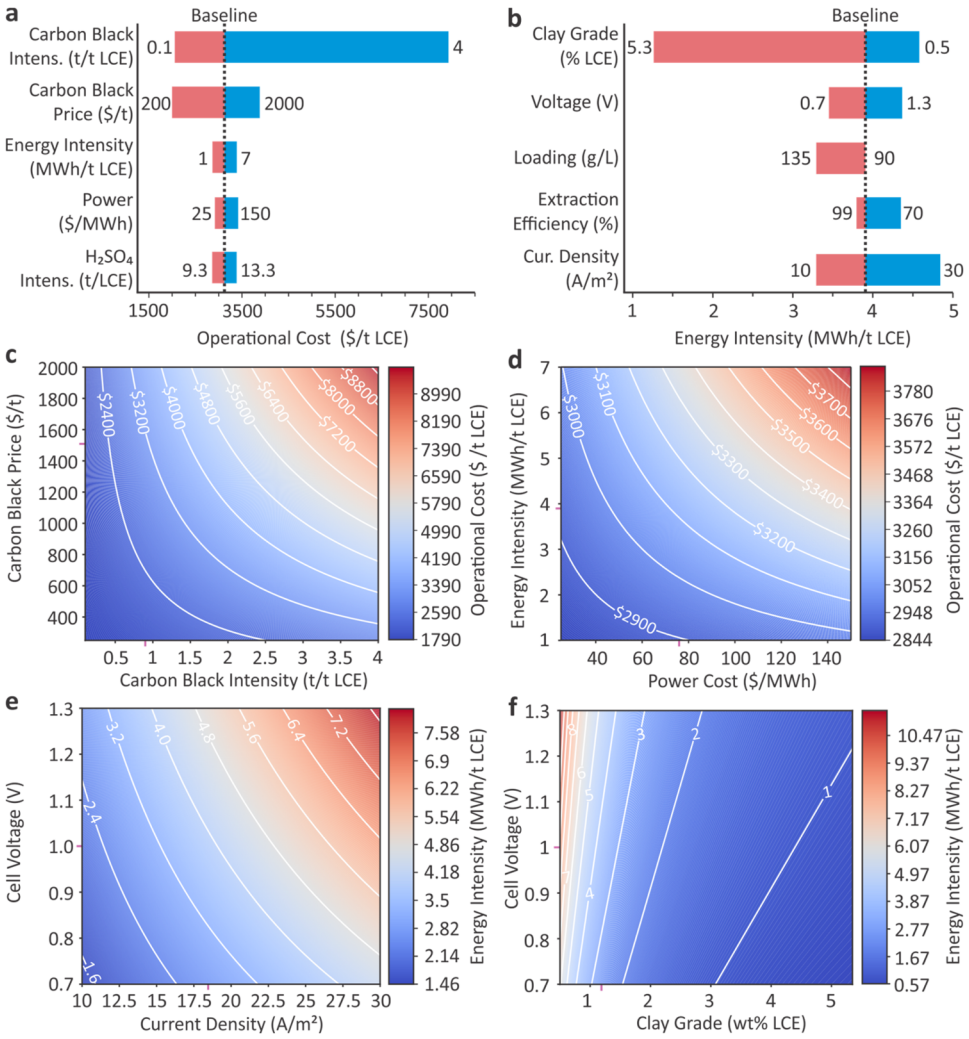

Figure 4. Cost and energy analysis of electrochemical leaching. (a) Sensitivity of the total cost of electrochemical lithium extraction relative to five model parameters. (b) Sensitivity of the energy intensity of electrochemical lithium extraction relative to five model parameters. An overview of all parameters and the base cases are described in Table S7. (c) Isolines of the total cost of electrochemical lithium extraction as a function of carbon black price and carbon black intensity. Purple ticks indicate the base case. (d) Isolines of the total cost of electrochemical lithium extraction as a function of energy intensity and power cost. Purple ticks indicate the base case. (e) Isolines of the energy intensity of electrochemical lithium extraction as a function of cell voltage and current density. Purple ticks indicate the baseline case from experimental data in this work. (f) Isolines of the energy intensity of electrochemical lithium extraction as a function of cell voltage and % LCE clay grade. Purple ticks indicate the base case.

represent a major expense at Thacker Pass.[26,66] These results accentuate the substantial energy and acid consumption benefits of electrochemical leaching, demonstrating that leveraging electrons instead of thermal energy (phonons) can improve efficiency across lithium feedstocks. These experimentally derived dependencies provide the inputs for the following energy- and cost-sensitivity analysis.

To assess the cost intensity of our leaching process and its competitiveness with industrial clay leaching methods, we compared operational costs, which included including electricity, reagents, and on-site fuel use, against two commercial facilities: one using concentrated sulfuric acid leaching[26] and the other employing sulfate roasting.[22] As shown in Figure S12, electrochemical leaching has an estimated operational cost of ~$3120 per t LCE based on batch testing parameters. Sulfuric acid leaching is slightly more expensive at ~$3990 per t LCE but decreases to ~$3460 per t LCE when accounting for energy savings from on-site sulfuric acid production, Table S6. Sulfate roasting has the lowest cost at ~$2750 per t LCE but requires the highest electricity and fuel consumption. Electrochemical leaching costs are primarily driven by reagent use, particularly carbon black, while electricity costs remain low. In contrast, sulfuric acid leaching is cost-intensive due to the purchase and transport of liquid sulfur and additional clay preprocessing reagents. Although sulfate roasting is the least expensive, its high energy demand presents trade-offs in sustainability and operational feasibility. Although still in a nascent stage of development, our initial operational cost estimates are in line with recently reported cost assessments of several lithium extraction facilities in the United States.[67]

We then performed a sensitivity analysis to identify key drivers and inform strategies to guide future development of our electrochemical leaching. For cost, we focused on operational expenses, including energy consumption, carbon black intensity (t/t LCE), sulfuric acid intensity (t/t LCE), and power cost ($/MWh). Baseline parameters included 11.3 t sulfuric acid/t LCE at $131/t, a power cost of $75/MWh, an

https://doi.org/10.1021/acs.est.5c11515
Environ. Sci. Technol. 2026, 60, 6162−6176

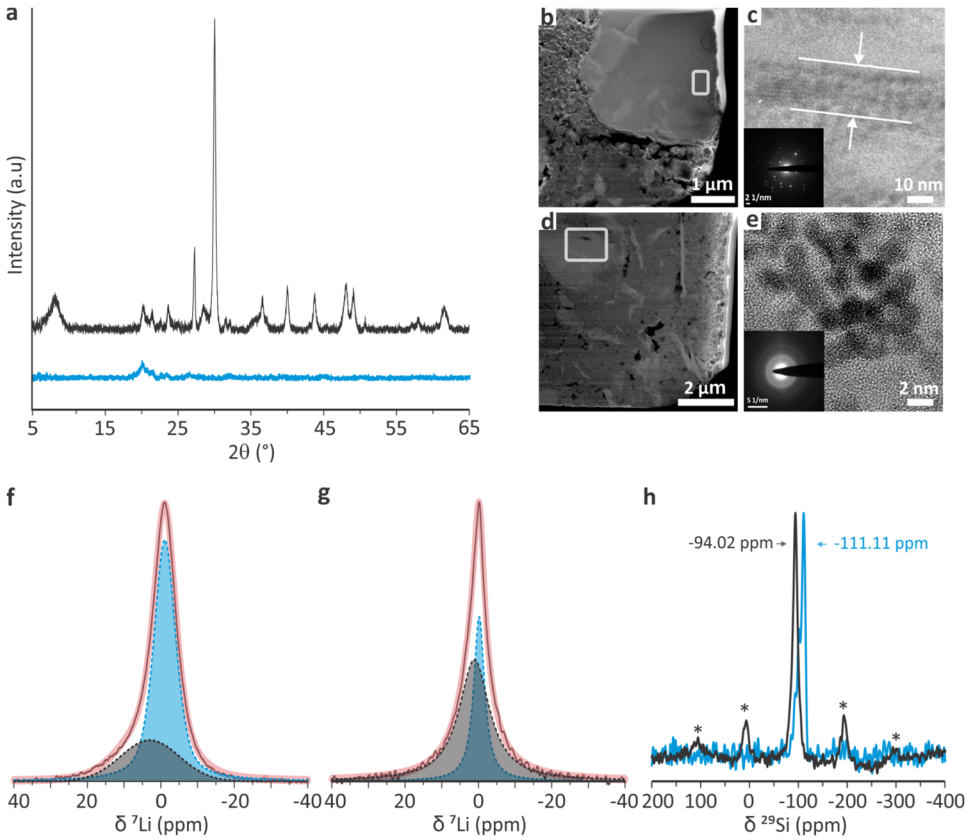

Figure 5. Post-mortem crystallographic and spectroscopic characterization of 90−10 HCSEs. (a) X-ray diffraction pattern of pristine HCSE (black) and leached HCSE (blue). (b) High-angle annular dark-field imaging (HAADF) STEM image of pristine HCSE. (c) HR-TEM of pristine HCSE; 10 nm resolution, with selected area electron diffraction (SAED) pattern (inset). (d) HAADF-STEM image of leached HCSE. (e) HR-TEM of leached HCSE; 2 nm resolution, with SAED pattern (inset). (f) Deconvoluted ^{7}Li SS-NMR spectra of pristine 90−10 HCSE; spectrum (black solid), model (red solid) −1.14 ppm (blue dotted and shaded blue), −2.98 ppm (black dotted and shaded black); plots show relative intensity. (g) Deconvoluted ^{7}Li SS-NMR spectra of leached 90−10 HCSE; spectrum (black solid), model (red solid) −0.16 ppm (blue dotted and shaded blue), −1.11 ppm (black dotted and shaded black); plots show relative intensity. (h) ^{29}Si SS-NMR spectra of pristine (black) and leached (blue) HCSEs; plots show relative intensity.

energy intensity of 3.91 MWh/t LCE, and a carbon black intensity of 0.8 t/t LCE at $1500/t. As shown in Figure 4a, total cost remained largely stable across most parameters but was highly sensitive to carbon black intensity and price. We note that the economic analysis presented here is intentionally restricted to operating expenses. Because the electrochemical leaching process is at an early technology readiness level and our experiments utilize batch reactors not representative of commercial architecture, the major determinants of capital expenditure (CapEx), including the design of a continuous-flow cell, electrode area scaling, current density targets, slurry circulation hardware, and electrode lifetime, cannot yet be specified with engineering accuracy. As a result, any CapEx estimate would be dominated by assumptions rather than data and could obscure, rather than clarify, the underlying scientific insights. For energy intensity, we analyzed the impact of clay grade (% LCE), voltage (V), slurry loading (g clay/L), extraction efficiency (%), and current density (A/m^2). Baseline parameters included a clay grade of 1.12 wt % LCE, a voltage of 1.0 V, a loading of 90 g clay/L, an extraction efficiency of 93%, and a current density of 17.7 A/m^2. As shown in Figure 4b, the most significant energy drivers were clay grade, and current density.

Using these sensitivity profiles, we constructed isolines to interpret how changes in the most influential drivers affect cost and energy intensity. As shown in Figure S13, even significant reductions in energy intensity have a minimal impact on total cost, whereas decreasing carbon black usage or price greatly improves economic feasibility. Figure 4c illustrates that halving the price of carbon black lowers total costs below $3000/t LCE for carbon black intensities of 2 t/t LCE. In the absence of price reductions, future process development will benefit from integrating carbon-black recovery and reuse. Similar separation challenges have been addressed in lithium-ion battery recycling, where carbon black is effectively recovered from composite slurries using flotation or centrifugal separation methods.[68,69] Although not demonstrated here, these established approaches suggest feasible routes for reducing carbon-black consumption in scaled implementations of electrochemical leaching.

Additionally, we examined the impact of power cost and energy intensity, the next most significant cost drivers, on total cost, Figure 4d. The narrow cost variation observed suggests adaptability to regional electricity prices. We emphasize that the economic analysis presented here encompasses only the extraction step, i.e., the electrochemical leaching of lithium into the aqueous phase. Downstream operations such as clarification and filtration of the leachate, impurity removal (e.g., Ca^{2+}, Mg^{2+}, Na^{+}, B-based species), concentration, and conversion to lithium carbonate or hydroxide are not included in the present

https://doi.org/10.1021/acs.est.5c11515
Environ. Sci. Technol. 2026, 60, 6162−6176

analysis. These unit operations are highly dependent on feedstock chemistry and process design and lie outside the scope of this early stage evaluation.

To evaluate energy intensity, we analyzed the effects of cell voltage, current density, lithium grade, and slurry loading. At a constant cell voltage, increases in current density raise the total charge passed during leaching and thus the energy intensity. Because lithium extraction does not scale linearly with current density under kinetically limited and mass-transport−limited conditions, higher current densities can reduce Faradaic efficiency and increase the charge consumed per unit Li extracted. Consequently, the total electrical energy required per tonne of LCE increases with current density even when voltage is held constant. This effect underlies the trend observed in Figure 4e. We then analyzed the impact of clay grade and cell voltage on energy intensity, Figure 4f. Lithium-bearing clays vary geographically, resulting in a wide range of lithium grades depending on deposit geology. The highest-grade deposit identified to date is at Thacker Pass, 1.68 wt % LCE. To capture both known and potential future deposits, we considered a broader range of 1−5 wt % LCE. The results show that even moderate grade increases significantly reduce energy intensity. For example, the 1.68 wt % grade at Thacker Pass lowers energy intensity to ∼2.5 MWh/t LCE at 1 V, a 36% reduction. Similarly, increasing slurry loading, Figure S14, could further decrease energy intensity to ≤2.5 MWh/t LCE. These findings suggest that optimizing cell design to reduce operating voltage while maintaining or increasing current density, along with process improvements for handling low-grade clays, will enhance energy efficiency and expand the feasibility of electrochemical leaching for abundant but lower-grade feedstocks.

Post-Mortem Characterization of HCSE after Electrochemical Leaching

To better understand structural changes during electrochemical leaching, we analyzed the spectroscopic, morphological, and crystallographic transformations of HCSEs postleaching. As shown in Figure 5a, XRD diffraction patterns became amorphous, confirming lattice deterioration and structural collapse. The disappearance of hectorite, calcite, and quartz reflections indicates significant lattice alterations, consistent with electrochemical data suggesting transition metal oxidation and ion deintercalation, which drive structural reformation. High-resolution XPS further examined the coordination and valency of Li, Fe, Si, and Mg, Figure S15a−d. Li 1s spectra confirmed the removal of Li 1s and Mg 2p core levels. Fe 2p spectra showed complete oxidation of Fe^{2+} to Fe^{3+}, aligning with the oxidizing electrochemical environment. Si 2p spectra exhibited a slight shift from 103 to 102 eV, along with the disappearance of the Mg 2s core level. However, Mg 1s spectra still showed core level excitations, confirming residual magnesium in the sample postleaching.

Morphological analysis of pristine and leached HCSEs further confirms the structural transformations induced by electrochemical leaching. Figure 5b presents a high-angle annular dark-field (HAADF) scanning transmission electron microscopy (STEM) image of pristine HCSE, with EDS mapping shown in Figure S16a. Silicon and oxygen exhibit uniform distribution, while Mg, Fe, and F are concentrated in specific regions, implying similar localization of Li. High-resolution transmission electron microscopy (HR-TEM) reveals a well-ordered structure with spherical HCSE grains, Figure 5c, and the selected area electron diffraction (SAED) pattern, Figure 5c inset, confirms crystallinity. The intensity plot of crystallites, Figure S17, shows three ordered layers spanning 3.69 nm (36.9 Å), consistent with XRD interplanar spacing measurements of 12.3 Å. Postleaching HAADF STEM images, Figure 5d, reveal significant fragmentation and pore formation, in contrast to the larger, intact structures observed in the pristine sample. STEM-EDS mapping of the leached HCSE residue, Figure S16b, indicates heterogeneous elemental distribution, differing from the uniformity in the pristine material. Focused ion beam scanning electron microscopy (FIB-SEM) further confirms nanopore formation, Figure S18. HR-TEM and SAED analysis confirm the transition from a well-ordered crystalline structure to an amorphous state with minor nanocrystalline regions, reinforcing the structural collapse observed after electrochemical leaching, Figure 5e inset.

We employed bulk characterization techniques, including ATR-FTIR and ^{29}Si and ^{7}Li solid-state NMR (SS-NMR), to monitor structural changes during electrochemical leaching. FTIR spectra were recorded every 3 h over 24 h, Figure S19, as IR spectroscopy is highly sensitive to subtle changes in the octahedral composition of smectites, including hectorite.[64,70,71] The pristine HCSE exhibited a strong Si−O symmetric stretching band at 1010 cm^{-1}, consistent with prior reports.[72] Three key spectral changes occurred during leaching. The emergence of a vibrational mode at 880 cm^{-1} appeared at 3 h and intensified over time, corresponding to vibrations of metal-O octahedral sites.[73] Its growth suggests significant changes in the coordination environment, possibly indicating the formation of a new iron silicate phase as hectorite delaminates and Li and Mg are displaced. Notably, a similar 880 cm^{-1} peak has been observed in acid-treated hectorite, attributed to bending vibrations from oxygen coordinated octahedral iron.[64] There was also a shift of the Si−O symmetric stretching band from 1010 cm^{-1} to ∼1050 cm^{-1}. This shift is consistent with the formation of amorphous SiO_2,[74] indicating lattice breakdown. The emergence of a new vibrational mode at ∼1175 cm^{-1} increased in intensity over time, eventually splitting into two asymmetric vibrations at longer leaching durations. This region aligns with alkali metal sulfate signatures, including Li_2SO_4,[75] suggesting that these peaks correspond to the release of alkali metal cations (Li, Mg, Na, K) from hectorite, which subsequently form sulfate or bisulfate salts.

The ^{7}Li NMR spectra of pristine and leached 90−10 HCSEs, Figure S20, show a broad peak centered between −1.5 and 0 ppm. Deconvolution revealed two lithium environments in both samples. In the pristine HCSE spectrum, Figure 5f, a tall peak appeared at −1.14 ppm with 43% Gaussian character, while a shorter, broad peak was observed at 2.98 ppm with 100% Gaussian character, Table S4. The high Gaussian character suggests inhomogeneities in the HCSE crystal lattice, with both sites exhibiting similar T_2 relaxation times (∼2 ms). These results align with previous ^{7}Li NMR studies on synthetic hectorite, which reported a peak near 0 ppm.[76] In contrast, the leached HCSE spectrum, Figure 5g, showed a significant signal reduction, consistent with ^{7}Li extraction. Deconvolution revealed a narrow peak at −0.16 ppm and a broader peak at 1.11 ppm, both with 0% Gaussian character and shorter T_2 times (<1 ms), indicating changes in lithium coordination due to electrochemical leaching. Despite the presence of Fe^{2+} and Fe^{3+} in both samples, the ^{7}Li chemical shifts remain within the diamagnetic range, centered around 0 ppm. Since para-

https://doi.org/10.1021/acs.est.5c11515
Environ. Sci. Technol. 2026, 60, 6162−6176

magnetic lithium exhibits chemical shifts in the hundreds of ppm, the precise assignment of individual Li peaks remains challenging.

The ^{29}Si NMR spectra provides insight into the coordination environment of silicon sites in HCSE, Figure 5h. Previous studies indicate that ^{29}Si chemical shifts between −90 and −95 ppm correspond to geminal silanols (Q^2), shifts around −100 ppm is associated with single silanols (Q^3), and shifts near −110 ppm represent siloxane bridges (Q^4).[77] In the pristine HCSE, a single isotropic ^{29}Si resonance appears at −94 ppm (Q^2). After leaching, the spectrum shifts, displaying an intense peak around −111 ppm (Q^4) and weaker resonances at −94 and −102 ppm (Q^2 and Q^3, respectively). This transformation indicates that silicon sites are converted from geminal silanols (Q^2) to siloxane bridges (Q^4) during the leaching process. This structural shift disrupts the SiO_4 tetrahedral network that forms hectorite, contributing to the amorphous nature of the leached material. The findings align with previous reports showing that the proportions of Q^n species in phyllosilicates depend on alkali metal concentration, with a reduction in alkali metals promoting Q^4 formation.[78] Additionally, the decrease in sideband intensity suggests a reduction in chemical shift anisotropy (CSA) of silicon sites, further supporting the loss of crystallinity and the emergence of an amorphous SiO_2 phase, as confirmed by FTIR and XRD.

The enhanced electrochemical activation observed in the slurry electrodes arises from the synergistic coupling of electronic, structural, and chemical processes that act within the hectorite lattice. Carbon black provides a continuous electronic percolation network around mineral particles, enabling the applied potential to penetrate the otherwise insulating clay and access Fe^{2+} centers embedded within the octahedral sheets. Once electronically addressable, Fe^{2+} undergoes anodic oxidation to Fe^{3+}, generating a localized positive charge that perturbs the charge balance and weakens the surrounding Mg−O and Fe−O coordination environment. Simultaneously, proton uptake, enabled by the acidic electrolyte, further destabilizes octahedral sites through partial dehydroxylation and protonation of surface oxygen atoms. These redox−proton-coupled modifications reduce the structural coherence of the trioctahedral sheet, lowering the energetic barrier for cation migration and enabling Li^+ and Mg^{2+} to be released from their coordination sites. As these processes propagate across the particle, the silicate framework loses long-range order, ultimately producing the amorphous, nanoporous residue observed experimentally. Importantly, this redox-driven lattice deconstruction does not occur in the absence of electronic percolation (as in the 100−0 composition), demonstrating that composite-enabled electron transfer is the prerequisite for initiating the mechanistic pathway leading to Li extraction.

Implications

Electrochemical leaching of hectorite is achieved through an iron-redox proton coupled lattice deconstruction pathway that results in the release of lithium and other alkaline ions. The process achieves a maximum lithium extraction efficiency of 93% after 24 h, a Faradaic efficiency of 77.2%, and an energy intensity of 3.91 MWh/t LCE, demonstrating significantly lower energy consumption compared to conventional methods. Our findings establish electrochemical leaching as an energy-efficient alternative to thermochemical lithium extraction, potentially enabling the utilization of previously uneconomical clay deposits. The ability to process low-grade clays with reduced economic and energy impact could help reshape global lithium supply chains, particularly in regions lacking high-grade spodumene or brine deposits. Beyond lithium, this approach may be adaptable for electrochemical leaching of other critical materials. Because the redox mediation and proton-coupled dissolution mechanism are generic to silicate, aluminate, and phosphate matrices, this electrified route can be extended to untapped resources of nickel, cobalt, gallium, and rare-earth elements, charting a scalable path toward low-carbon, room-temperature metallurgy, further expanding its potential impact on sustainable resource extraction.

The leach residue generated after electrochemical extraction consists primarily of an amorphous, silica-rich solid matrix, as indicated by XRD, FTIR, XPS, and electron microscopy. Transition-metal content is low, and iron is present almost exclusively as Fe^{3+}, with no evidence of soluble or redox-active iron species remaining. Because alkali ions and Mg^{2+} are largely removed during leaching, the residue resembles acid-treated clay tailings commonly produced in hydrometallurgical operations and is expected to be chemically stable and nonhazardous under typical disposal conditions. Although a detailed environmental assessment is beyond the scope of this work, the absence of introduced heavy metals or persistent organic species suggests minimal toxicity concerns. In principle, the silica-rich residue could be repurposed as a low-value industrial material (e.g., filler, pozzolanic additive, or mine backfill), and the carbon black fraction may be recoverable via flotation or centrifugation. These possibilities require further study, but the residue composition does not indicate inherent environmental hazards.

Our cost and energy modeling results indicate that electrochemical leaching is highly adaptable across a range of operational conditions, but significant challenges remain in improving kinetics and enabling industrial scalability. The current densities demonstrated here (0.84−1.77 mA cm^{-2}) are 2 orders of magnitude below industrial electrowinning practice, and the 24-h leaching time required to achieve 93% Li extraction is unlikely to be practical at scale. Addressing these limitations will require increased current density, shorter residence times, and reactor designs that promote more efficient particle−electrode interactions. Several process-intensification pathways, including continuous-flow slurry reactors (e.g., parallel-plate flow-by, interdigitated channels, packed or porous anode geometries), circulating-slurry or fluidized-bed electrochemical reactors, and high-surface-area MMO anodes (mesh, foam, reticulated structures), offer promising routes to increase reactive surface area, improve mass transfer, and maintain stable particle suspension. Additional strategies such as bipolar or stacked cell configurations, electronically conductive scaffolds, or redox-mediating additives may further enhance effective current density while keeping cell voltages low.

The stability of the slurry electrode during electrochemical leaching is supported by reproducible voltammetric behavior, stable rheology across relevant loadings, and the absence of progressive electrochemical degradation over extended operation. While the mineral phase undergoes intentional lattice deconstruction, the conductive carbon network remains electronically active throughout leaching. Because carbon black intensity emerges as a major cost driver, implementing recovery and reuse methods such as flotation or centrifugation

https://doi.org/10.1021/acs.est.5c11515
Environ. Sci. Technol. 2026, 60, 6162−6176

will also be essential as throughput increases. Ultimately, scaling to larger continuous-flow demonstrations will be critical to validate the energy and cost advantages of this process, and the engineering approaches outlined here illustrate potential pathways for translating the mechanistic insights gained in this study into viable industrial technology.

Despite clays having wide geographic distribution and accounting for ~7% of global lithium resources,[20] large-scale commercial ventures remain limited. Outside of a several emerging operations in the western United States and a proposed project in Serbia, there are no other commercial ventures and there is even less data available to benchmark their feasibility against brine salar and spodumene-based lithium production. We hope these results serve as a basis for reconsidering the economic potential of clay-based lithium extraction as well as highlighting the broader promise of electrochemical ore leaching strategies.

MATERIALS AND METHODS

Materials

Hectorite was supplied from the Rio Tinto US Borax Mine in Boron, CA and carbon black (Vulcan XC-72R) was purchased from the Fuel Cell Store. Concentrated sulfuric acid (99.9%) was purchased from Sigma-Aldrich.

HCSEs Preparation

The hectorite carbon black composite powders were prepared by adding together the appropriate wt % ratios of hectorite gangue and carbon black (100−0, 95−5, 90−10, 70−30, and 50−50). The mixtures were then ball milled for 15 min using. The crystallinity of the composite material was confirmed after ball milling (Figure S2). Slurry electrodes were then prepared by mixing the desired material loading with 0.125 M sulfuric acid and shear mixed for 30 min.

Electrochemical Characterizations

DC and AC conductivity/impedance measurements were collected using a custom-designed flow cell consisting of two 0.75 mm-thick channels. Gold current collectors were utilized in all conductivity experiments to minimize the contact resistance and other cell-related external effects. A single-channel configuration (i.e., no separator) with a 3 mm-thick latex gasket was used, similar to the ones depicted in previous work.[79] After mixing of the HCSEs, all samples were collected from their vials using a 1 mL pipet and manually transferred to the flow cells to ensure full coverage of the current collector surface prior to the cell assembly. Cells were tightened to the same pressure for each experiment using a torque wrench. DC and AC tests of the HCSEs was measured under static conditions (i.e., no-flow) using a Gamry Interface 1010E potentiostat. Under direct current conditions, a constant voltage was applied to the slurry electrodes for 10 min, and the resulting current was measured at 0.25, and 0.5 V. After reaching a steady-state current value, the resistance of the slurry electrodes was averaged over the different voltage values using Ohm's law. Then, the resistances were converted into intrinsic conductivity values using established relationships between cell geometry and resistivity.[79] Electrochemical impedance spectroscopy (EIS) was also performed in a wide frequency range (10^{-3}−10^{4} Hz) to generate Bode plots and understand the impact of the particle morphology and concentration on the interfacial and bulk electron conduction processes.

CV and LSV and leaching experiments were performed in a glass batch cell will a Teflon cover where working electrode, counter electrode and reference electrodes are immersed into the solution (Figure S9). The total cell volume was 25 mL of 0.125 M H_2SO_4 and HCSE concentration loadings were 100 g/L. A Ag/AgCl electrode was used as reference, a platinum wire as a counter and an acid-resistant mixed metal oxide (Ti/Ta/Ir) cut was used as the working electrode. The immersed area of the working electrode was measured to be 2.1545 cm^2.

CV and LSV curves of all HCSE compositions were collected at a scan rate of 0.5 mV/s under static conditions using a Gamry Interface 1010E potentiostat. Acid concentration dependence LSVs were performed the same as described above, but starting with a concentration 0.025 M H_2SO_4 followed by titrations of acid corresponding to concentrations of 0.05, 0.075, 0.1, 0.125, 0.15, 0.175, 0.2 M H_2SO_4.

Leaching experiments were performed over a 24-h duration under constant stirring using a magnetic stir bar at potentials of 0.7, 0.8, 0.9, and 1.0 V. Aliquots were sampled using a 1 mL syringe and filtered using a syringe filter and the filtrate collected for IC analysis. Acid leaching control tests were performed using the same setup but without the application of potential.

Rheology

Hectorite and carbon black in a ratio of 90−10 was ball-milled for 15 min and immersed in 5 mL of 0.125 M sulfuric acid aqueous solution with concentrations of 25 g/L, 50 g/L, 100 g/L, and 150 g/L. Solutions were shear mixed for 30 min prior to analysis. Rheological data was collected using a HR-2 rheometer (Discovery Series from TA Instruments) with a 40 mm parallel plate accessory (Peltier plate steel). Stress and Strain were measured using flow sweep as a function of shear rate ranging from 1 s^{-1} to 1000 s^{-1}, temperature held at 25 °C, and a step time 65s. Experiments were performed in triplicate.

XRD

Determination of bulk crystalline mineral composition of pristine HCSE electrode and leached HCSE was obtained from powder XRD patterns using a Bruker diffractometer with a Cu source. Diffraction patterns were collected from 5 to 70° 2θ with 0.01 frames per 0.5 s at a rotation of 5 rpm. Data was then fitted using diffract EVA software.

XPS Experiments and EELS

Pristine and leached HCSEs were analyzed by XPS vertical analysis. After the conclusion of the leaching tests 10 mL of the HCSE were filtered under vacuum using a glass frit. The residue material was washed with excess deionized water. Both pristine and leched samples were then dried in a vacuum oven at 50 °C for 48 h to remove any residual moisture. The samples were then mounted onto sample holder and 3 points were chosen for analysis. Spectra were collected using a Thermo-Fisher K-Alpha Plus XPS/UPS employing a monochromatic Al X-ray source (1.486 eV). Li 1s, Na 1s, Mg 1s, Fe 2p, Si 2p, high resolution spectra were then collected. The spectra were acquired using a spot size of 400 μm and constant pass energy. A combined low-energy electron/ion flood source was used for charge neutralization. A dual monatomic and gas cluster Argon ion source for depth profiling and sample cleaning. The spectra were referenced to the adventitious carbon reference peak at 284.8 eV and were analyzed using Casa XPS software. Baseline corrections were performed using the Shirley background subtraction. Experiments were performed in triplicate using three different polarized and pristine HCSE samples. Leached HCSE samples were analyzed by Electron energy-loss spectroscopy (EELS) based on the 200 kV FEI monochromated F20 UT Tecnai with an energy resolution of 0.5 eV.

ATR-FTIR Spectroscopy

Attenuated total reflectance Fourier transform infrared (ATR-FTIR) spectroscopy measurements were analyzed using a Thermo Electron Nicolet 5700 FTIR with attachment with diamond crystal attachment. The FTIR had a collection range of 2000−800 cm^{-1} and were averaged over 40 scans with a spectral resolution of 4 cm^{-1}. Aliquots from leaching experiments were taken a time 0−24 h and placed onto the diamond crystal and covered with a glass slide and pressed to a constant pressure. Spectra were then collected and processed using Omni software.

STEM-EDX, FIB-SEM, and HRTEM

A FEI Phenom tabletop scanning electron microscope was used to obtain high resolution images of HCSEs. The local nanostructure of the pristine and leached HCSEs was investigated with HRTEM (Titan X 60−300, FEI), operating at 200 kV. The sample was thinned by FIB (Ga ion beam on Helios G4 UX. FEI) after a 1 μm Pt coating

https://doi.org/10.1021/acs.est.5c11515
Environ. Sci. Technol. 2026, 60, 6162−6176

for surface protection. The structural analysis, including high-angle annular dark-field (HAADF)-STEM, was conducted using a probe-side aberration-corrected TEM. The elemental mapping was collected from EDS (Bruker) equipped within the TEM at 300 kV. Cross-sectioned images were obtained by using the FIB-SEM technique (Helios G4 UX dual beam, FEI). Pt was used to make a protective layer for the samples before milling, and Ga^+ ions are used for milling.

Solid State NMR

^{7}Li solid-state NMR (ssNMR) spectra were recorded at 9.4 T (400 MHz for ^{1}H) using a Bruker BioSpin spectrometer equipped with an Avance IV NEO console and a 3.2 mm double resonance HX magic angle spinning (MAS) probe tuned to ^{7}Li (155.5 MHz). Samples were loaded in 3.2 mm zirconia rotors, closed using Vespel caps, and spun at the magic angle at 24 kHz using dry nitrogen. Sample mass varied between 28.8 and 47.9 mg. ^{7}Li spectra were obtained with a rotor-synchronized Hahn echo ($90° - \tau - 180° - \tau - AQ$, with τ = 1 rotor period) using a 90° radio frequency pulse of 3.475 μs and a recycle delay of 5*T_1 to allow for full relaxation of nuclear spins. T_1 and T_2 relaxation experiments were measured for each sample using a saturation recovery experiment (delays ranging from 10 μs to 1 s) or by recording spin−echo spectra at different echo durations (from 83.3 μs to 16.7 ms), respectively.

^{29}Si ssNMR spectra were recorded at 11.7 T (500 MHz for ^{1}H) Bruker BioSpin spectrometer equipped with a Bruker Avance I console and 4 mm ^{1}H/BB CP-MAS probe tuned to ^{29}Si (99.4 MHz). Samples were loaded in 4.0 mm zirconia rotors, closed using Kel-F caps, and spun at the magic angle at 10 kHz using dry nitrogen. Sample weight varied between 100 and 200 mg. ^{29}Si spectra were obtained using a rotor-synchronized Hahn echo ($90° - \tau - 180° - \tau - AQ$, with τ = 1 rotor period) using a 90° radio frequency pulse of 2.75 μs. Recycle delays of 15, 30, 50, and 40 s were used for pristine, leached 90−10, leached 100−0, and leached 50−50 HCSE, respectively.

^{7}Li chemical shift was referenced with respect to aqueous 1 M LiCl at δ_{iso} (^{7}Li) = 0 ppm. ^{29}Si chemical shift was referenced with respect to tetramethylsilane (TMS) using the geminal silanol resonance of kaolinite as a secondary external reference at δ_{iso} (^{29}Si) = −91.5 ppm. All solid-state NMR data were processed using Bruker TopSpin 4.4.1 and deconvoluted with DMFIT software.[80]

ICP-MS

Samples of hectorite were dried and digested with a mixture of concentrated nitric acid and concentrated hydrochloric acid at 220 °C using a microwave system (Multiwave 3000, Anton Paar). The samples and acid(s) were placed in a fluoropolymer microwave vessel. The vessel was sealed and heated in the microwave. The temperature of each sample increased to 220 °C in approximately 15 min and remained at 220 °C for 60 min digestion period. After cooling, the vessel contents were filtered with a 0.45 μm PTFE membranes and then diluted with a 2% nitric acid to the appropriate volumes for ICP-MS analysis using an Agilent HPLC-ICP-MS, n = 3.

Ion Chromatography

Ion Chromatography measurements were collected on a Thermo Scientific Dionex Ion Chromatography System using a Dionex IonPac CS16 (3 mm × 250 mm) cation exchange column. During leaching experiments, aliquots were syringed from the electrolyte solution using a 1 mL syringe, filtered using a syringe filter and collected in scintillation vials. 0.05 mL of the filtered leachate was then diluted with deionized water to a total volume of 5 mL (100× dilution) in Thermo Scientific auto select sure start vials. Samples were then mounted on the IC sample holder and data was autonomously collected and referenced against Li calibration standards.

Acknowledgments: We thank Rio Tinto US Borax for supplying the hectorite gangue used in this study. We thank Aepnus Technology for the use of their Ion Chromatography instrument and for the assistance with conductivity cell design and fabrication. Lawrence Berkeley National Laboratory is supported by the U.S. Department of Energy under Contract No. DE-AC02−05CH11231.

■ ASSOCIATED CONTENT

Data Availability Statement

All data are available in the main text and the Supporting Information.

Supporting Information

The Supporting Information is available free of charge at https://pubs.acs.org/doi/10.1021/acs.est.5c11515.

XPS survey of hectorite gangue, XRD of ball-milled HCSE vs pristine HCSE, conductivity of HCSEs with varying amounts of carbon black additive, LSV of 0.125 M H_2SO_4, Butler−Volmer LSV fit of all HCSE compositions, calculated heterogeneous rate constants vs HCSE composition, LSV of 90−10 HCSE with increasing acid concentration, thermodynamic square of reaction pathways, photograph of experimental setup for batch cell leaching experiments, rheology of HCSE, charge vs potential and FE calculations for leaching tests of 90−10 HCSE, cost estimate of electrochemical leaching and industrial leaching methods, energy intensity and carbon black intensity total cost isolines, cell voltage and slurry loading energy intensity isolines, Li 1s, Fe 2p, Mg 1s, and Si 2p high resolution XPS of leached HCSEs, STEM-EDS elemental mapping of pristine and leached HCSEs, intensity plot of crystallite from SAED pattern, SEM-FIB images of pristine HCSE and leached HCSE, ATR FTIR spectra of HCSE residues, solid state NMR ^{7}Li NMR spectra of pristine and leached HCSE, EELS Li K-edge spectrum of leached HCSE, ICP-MS elemental composition of hectorite gangue, lithium composition in the leachate during electrochemical leaching, full composition of leachate after 24 h of electrochemical leaching at 1 V, ^{7}Li NMR fitting parameters, calculation of energy intensity for electrochemical leaching, comparison of energy, materials and cost to produce 1 metric tonne of Li_2CO_3 from traditional commercial processes and electrochemical leaching, parameters considered for cost and energy sensitivity analysis (PDF)

Cost intensity python script_enrgy intensity vs CB intensity_matplot (TXT)

Cost intensity python script_CB cost vs CB intensity_matplot (TXT)

Cost intensity python script_enrgy intensity vs power cost_matplot (TXT)

Energy intensity_matplot script_current density vs cell voltage (TXT)

Energy intensity_matplot script_material grade vs cell voltage (TXT)

■ AUTHOR INFORMATION

Corresponding Authors

Andrew Z. Haddad − *Energy Storage and Distributed Resources Division, Lawrence Berkeley National Laboratory, Berkeley, California 94720, United States;* orcid.org/0000-0002-9206-3505; Email: azhaddad@lbl.gov

Robert Kostecki − *Energy Storage and Distributed Resources Division, Lawrence Berkeley National Laboratory, Berkeley, California 94720, United States;* orcid.org/0000-0002-4014-8232; Email: r_kostecki@lbl.gov

https://doi.org/10.1021/acs.est.5c11515
Environ. Sci. Technol. 2026, 60, 6162−6176

Authors

Hyungyeon Cha − *Energy Storage and Distributed Resources Division, Lawrence Berkeley National Laboratory, Berkeley, California 94720, United States;* orcid.org/0009-0004-7457-8400

Sahand Adibnia − *Energy Storage and Distributed Resources Division, Lawrence Berkeley National Laboratory, Berkeley, California 94720, United States;* orcid.org/0000-0003-4767-7951

Xander B. Fleming − *College of Chemistry, University of California Berkeley, Berkeley, California 94720, United States*

Liam McDonough − *Energy Storage and Distributed Resources Division, Lawrence Berkeley National Laboratory, Berkeley, California 94720, United States*

Floria Li − *Energy Storage and Distributed Resources Division, Lawrence Berkeley National Laboratory, Berkeley, California 94720, United States*

Siva Bandaru − *Energy Storage and Distributed Resources Division, Lawrence Berkeley National Laboratory, Berkeley, California 94720, United States*

Raynald Giovine − *College of Chemistry, University of California Berkeley, Berkeley, California 94720, United States;* orcid.org/0000-0002-7208-6929

Chaochao Dun − *The Molecular Foundry, Lawrence Berkeley National Laboratory, Berkeley, California 94720, United States;* orcid.org/0000-0002-3215-6478

Garrett Pohlman − *Energy Storage and Distributed Resources Division, Lawrence Berkeley National Laboratory, Berkeley, California 94720, United States*

Lukas Hackl − *Energy Storage and Distributed Resources Division, Lawrence Berkeley National Laboratory, Berkeley, California 94720, United States*

Bilen Akuzum − *Energy Storage and Distributed Resources Division, Lawrence Berkeley National Laboratory, Berkeley, California 94720, United States*

Jeffrey J. Urban − *The Molecular Foundry, Lawrence Berkeley National Laboratory, Berkeley, California 94720, United States;* orcid.org/0000-0003-4909-2869

Complete contact information is available at: https://pubs.acs.org/10.1021/acs.est.5c11515

Author Contributions

Conceptualization: A.Z.H., R.K. Methodology: A.Z.H., R.K. Investigation: A.Z.H., H.C., S.A., X.F., R.G., L.M., C.D., F.L., S.B., G.P. Visualization: A.Z.H., H.C., S.A. Funding acquisition: A.Z.H. Project administration: A.Z.H. Supervision: A.Z.H., R.K. Writing—original draft: AZH writing—review and editing: all authors

Funding

This work was supported by Lawrence Berkeley National Laboratory's Lab Directed Research and Development (LDRD) grant and by the Vehicle Technologies Office of the Department of Energy under contract No. DE-AC02-05CH11231, under the Battery Materials Research program. Work at the Molecular Foundry was supported by the Office of Basic Energy Sciences of the U.S. Department of Energy under contract No. DE-AC02−05CH11231.

Notes

The authors declare the following competing financial interest(s): A.Z.H. and R.K. are inventors on a United States patent (application number 63/568,323, patent pending).

REFERENCES

(1) Henze, V. Long-Term Energy Storage Outlook *BloombergNEF* 2019.

(2) DOE. *United States National Blueprint for Lithium Batteries 2030−2021*, 2021.

(3) Olivetti, E. A.; Ceder, G.; Gaustad, G. G.; Fu, X. Lithium-Ion Battery Supply Chain Considerations: Analysis of Potential Bottlenecks in Critical Metals. *Joule* **2017**, *1* (2), 229−243.

(4) Battistel, A.; Palagonia, M. S.; Brogioli, D.; La Mantia, F.; Trócoli, R. Electrochemical Methods for Lithium Recovery: A Comprehensive and Critical Review. *Adv. Mater.* **2020**, *32* (23), No. 1905440.

(5) Ambrose, H.; Kendall, A. Understanding the future of lithium: Part 1, resource model. *J. Ind. Ecol.* **2020**, *24* (1), 80−89.

(6) Haddad, A. Z.; Hackl, L.; Akuzum, B.; Pohlman, G.; Magnan, J.-F.; Kostecki, R. How to make lithium extraction cleaner, faster and cheaper—in six steps. *Nature* **2023**, *616*, 245−248.

(7) *Mineral Commodity Summaries*, Reston, VA, 2021; p 200.

(8) Stringfellow, W. T.; Dobson, P. F. Technology for the Recovery of Lithium from Geothermal Brines. *Energies* **2021**, *14* (20), No. 6805.

(9) Flexer, V.; Baspineiro, C. F.; Galli, C. I. Lithium recovery from brines: A vital raw material for green energies with a potential environmental impact in its mining and processing. *Sci. Total Environ.* **2018**, *639*, 1188−1204.

(10) Swain, B. Recovery and recycling of lithium: A review. *Sep. Purif. Technol.* **2017**, *172*, 388−403.

(11) Baudino, L.; Santos, C.; Pirri, C. F.; La Mantia, F.; Lamberti, A. Recent Advances in the Lithium Recovery from Water Resources: From Passive to Electrochemical Methods. *Adv. Sci.* **2022**, *9* (27), No. 2201380.

(12) Paranthaman, M. P.; Li, L.; Luo, J.; Hoke, T.; Ucar, H.; Moyer, B. A.; Harrison, S. Recovery of Lithium from Geothermal Brine with Lithium−Aluminum Layered Double Hydroxide Chloride Sorbents. *Environ. Sci. Technol.* **2017**, *51* (22), 13481−13486.

(13) *Mineral Commodity Summaries*; US Geological Survey, 2022.

(14) Ellestad, R. B.; Milne, L. K. Method of Extracting Lithium Values from Spodumene Ores. US Patent US2516109A, 1950.

(15) Castor, S. B.; Henry, C. D. Lithium-Rich Claystone in the McDermitt Caldera, Nevada, USA: Geologic, Mineralogical, and Geochemical Characteristics and Possible Origin. *Minerals* **2020**, *10* (1), No. 68.

(16) Benson, T. R.; Coble, M. A.; Rytuba, J. J.; Mahood, G. A. Lithium enrichment in intracontinental rhyolite magmas leads to Li deposits in caldera basins. *Nat. Commun.* **2017**, *8* (1), No. 270.

(17) Xie, R.; Zhao, Z.; Tong, X.; Xie, X.; Song, Q.; Fan, P. Review of the research on the development and utilization of clay-type lithium resources. *Particuology* **2024**, *87*, 46−53.

(18) Putzolu, F.; Armstrong, R. N.; Herrington, R. J. Jadarite's unique recipe. *Nat. Geosci.* **2025**, *18* (6), 454.

(19) Benson, T. R.; Coble, M. A.; Dilles, J. H. Hydrothermal enrichment of lithium in intracaldera Illite-bearing claystones. *Sci. Adv.* **2023**, *9* (35), No. eadh8183.

(20) Zhao, H.; Wang, Y.; Cheng, H. Recent advances in lithium extraction from lithium-bearing clay minerals. *Hydrometallurgy* **2023**, *217*, No. 106025.

(21) Crocker, L. *Lithium and Its Recovery from Low-Grade Nevada Clays*; U.S. Department of the Interior Bureau of Mines, 1988.

(22) Joel Carrasco, H. W.; Lane, G.; Martin, P. *Technical Report on the Feasibility Study for the Sonora Lithium Project*; Bacanora Minerals Ltd.: Mexico, 2018.

(23) Komadel, P.; Madejová, J.; Janek, M.; Gates, W. P.; Kirkpatrick, R. J.; Stucki, J. W. Dissolution of Hectorite in Inorganic Acids. *Clays Clay Miner.* **1996**, *44* (2), 228−236.
(24) Fluor Enterprises, I., IONEER USA Corp. *Rhyolite Ridge Lithium-Boron Project Definitive Feasibility Study (DFS) Report*, 2020.
(25) Patwardhan, A.; Shinde, S.; Wattenbarger, A. Lithium Carbonate Production Process and Apparatus. US Patent US12,275,644, 2020.
(26) Roth, D.; Tahija, L.; Iasillo, E.; Martina, K.; Chow, B.; Mutler, W.; Bahe, K.; Kaplan, P.; Cluff, T.; Shannon, B. *Feasibility Study, National Instrument 43−101*, Technical Report for the Thacker Pass Project Humboldt County Humboldt County, Nevada, USA, 2022.
(27) Crop., C. D. Clayton Valley Lithium Project, Nevada. https://www.cypressdevelopmentcorp.com/projects/nevada/clayton-valley-lithium-project-nevada/. (accessed March 19, 2020).
(28) Kelly, J. C.; Wang, M.; Dai, Q.; Winjobi, O. Energy, greenhouse gas, and water life cycle analysis of lithium carbonate and lithium hydroxide monohydrate from brine and ore resources and their use in lithium ion battery cathodes and lithium ion batteries. *Resour., Conserv. Recycl.* **2021**, *174*, No. 105762.
(29) Mousavinezhad, S.; Fahimi, A.; Sharifian, S.; Vahidi, E. Sustainable lithium production from sedimentary rock deposits: Carbon reduction and EV synergies. *Resour. Conserv. Recycl.* **2025**, *218*, No. 108271.
(30) Diaz, L. A.; Clark, G. G.; Lister, T. E. Optimization of the Electrochemical Extraction and Recovery of Metals from Electronic Waste Using Response Surface Methodology. *Ind. Eng. Chem. Res.* **2017**, *56* (26), 7516−7524.
(31) Jin, W. Towards source reduction and green sustainability of metal-bearing waste streams: The electrochemical processes. *Electrochim. Acta* **2021**, *374*, No. 137937.
(32) Diaz, L. A.; Lister, T. E.; Parkman, J. A.; Clark, G. G. Comprehensive process for the recovery of value and critical materials from electronic waste. *J. Cleaner Prod.* **2016**, *125*, 236−244.
(33) Rai, V.; Liu, D.; Xia, D.; Jayaraman, Y.; Gabriel, J.-C. P. Electrochemical Approaches for the Recovery of Metals from Electronic Waste: A Critical Review. *Recycling* **2021**, *6* (3), No. 53.
(34) Makarova, I.; Soboleva, E.; Osipenko, M.; Kurilo, I.; Laatikainen, M.; Repo, E. Electrochemical leaching of rare-earth elements from spent NdFeB magnets. *Hydrometallurgy* **2020**, *192*, No. 105264.
(35) Diaz, L. A.; Strauss, M. L.; Adhikari, B.; Klaehn, J. R.; McNally, J. S.; Lister, T. E. Electrochemical-assisted leaching of active materials from lithium ion batteries. *Resour. Conserv. Recycl.* **2020**, *161*, No. 104900.
(36) Jang, Y.; Hou, C.-H.; Kwon, K.; Kang, J. S.; Chung, E. Selective recovery of lithium and ammonium from spent lithium-ion batteries using intercalation electrodes. *Chemosphere* **2023**, *317*, No. 137865.
(37) Martens, E.; Prommer, H.; Sprocati, R.; Sun, J.; Dai, X.; Crane, R.; Jamieson, J.; Tong, P. O.; Rolle, M.; Fourie, A. Toward a more sustainable mining future with electrokinetic in situ leaching. *Sci. Adv.* **2021**, *7* (18), No. eabf9971.
(38) Zhang, H.; Han, Y.; Lai, J.; Wolf, J.; Lei, Z.; Yang, Y.; Shi, F. Direct extraction of lithium from ores by electrochemical leaching. *Nat. Commun.* **2024**, *15* (1), No. 5066.
(39) Lee, H. Y.; Kim, S. G.; Oh, J. K. Electrochemical leaching of nickel from low-grade laterites. *Hydrometallurgy* **2005**, *77* (3), 263−268.
(40) Linnemann, J.; Kanokkanchana, K.; Tschulik, K. Design Strategies for Electrocatalysts from an Electrochemist's Perspective. *ACS Catal.* **2021**, *11* (9), 5318−5346.
(41) Srikanth, V.; Roy, R.; Komarneni, S. Acoustic-wave stimulation of the leaching of layer silicates. *Mater. Lett.* **1992**, *15* (1), 127−129.
(42) Okonkwo, E. G.; Wheatley, G.; Liu, Y.; He, Y. A cavitation enabled green leaching of metals from spent lithium-ion batteries. *Chem. Eng. Process.—Process Intensif.* **2024**, *202*, No. 109850.
(43) Sadoway, D. R. New opportunities for metals extraction and waste treatment by electrochemical processing in molten salts. *J. Mater. Res.* **1995**, *10* (3), 487−492.
(44) Li, M.; Liu, C.; Ding, A.; Xiao, C. A review on the extraction and recovery of critical metals using molten salt electrolysis. *J. Environ. Chem. Eng.* **2023**, *11* (3), No. 109746.
(45) Qu, J.; Chen, X.; Xie, H.; Gao, S.; Wang, D.; Yin, H. Anode electrolysis of sulfides. *Proc. Natl. Acad. Sci. U.S.A.* **2022**, *119* (31), No. e2202884119.
(46) Haddad, A. Z.; Cha, H.; McDonough, L.; Dun, C.; Pohlman, G.; Urban, J. J.; Kostecki, R. Electrochemical lithium extraction from hectorite ore. *Commun. Chem.* **2024**, *7* (1), No. 285.
(47) Madejová, J.; Bujdák, J.; Janek, M.; Komadel, P. Comparative FT-IR study of structural modifications during acid treatment of dioctahedral smectites and hectorite. *Spectrochim. Acta, Part A* **1998**, *54* (10), 1397−1406.
(48) Hazen, R. M.; Sverjensky, D. A.; Azzolini, D.; Bish, D. L.; Elmore, S. C.; Hinnov, L.; Milliken, R. E. Clay mineral evolution. *Am. Mineral.* **2013**, *98* (11−12), 2007−2029.
(49) Misaelides, P.; Macásek, F.; Pinnavaia, T. J.; Colella, C. *Natural Microporous Materials in Environmental Technology*; Springer: Netherlands, 2012.
(50) Komadel, P.; Madejová, J.; Bujdák, J. Preparation and Properties of Reduced-Charge Smectites — A Review. *Clays Clay Miner.* **2005**, *53* (4), 313−334.
(51) Kloprogge, J. T.; Komarneni, S.; Amonette, J. E. Synthesis of Smectite Clay Minerals: A Critical Review. *Clays Clay Miner.* **1999**, *47* (5), 529−554.
(52) Zhang, J.; Zhou, C. H.; Petit, S.; Zhang, H. Hectorite: Synthesis, modification, assembly and applications. *Appl. Clay Sci.* **2019**, *177*, 114−138.
(53) Kalo, H.; Milius, W.; Breu, J. Single crystal structure refinement of one- and two-layer hydrates of sodium fluorohectorite. *RSC Adv.* **2012**, *2* (22), 8452−8459.
(54) Foshag, W. F.; Woodford, A. O. Bentonitic magnesian clay mineral from California. *Am. Mineral.* **1936**, *21* (4), 238−244.
(55) Hernandez, L.; Hernandez, P.; Lorenzo, E.; Ferrera, Z. S. Comparative study of the electrochemical behaviour of sepiolite and hectorite modified carbon paste electrodes in the determination of dinocap. *Analyst* **1988**, *113* (4), 621−623.
(56) IJdo, W. L.; Kemnetz, S.; Benderly, D. An infrared method to assess organoclay delamination and orientation in organoclay polymer nanocomposites. *Polym. Eng. Sci.* **2006**, *46* (8), 1031−1039.
(57) Costanzo, P. M.; Norris, J.; Giese, R.; Van Oss, C. J. In *Surface Energies of Some Smectite Clay Minerals*; Proceedings of the 9th international Clay Conference, Strasbourg, 1989. Vol II: Surface chemistry. Structure and mixed layering of clays, 1990; pp 33−41.
(58) Akuzum, B.; Singh, P.; Eichfeld, D. A.; Agartan, L.; Uzun, S.; Gogotsi, Y.; Kumbur, E. C. Percolation Characteristics of Conductive Additives for Capacitive Flowable (Semi-Solid) Electrodes. *ACS Appl. Mater. Interfaces* **2020**, *12* (5), 5866−5875.
(59) Bard, A. J.; Faulkner, L. R.; White, H. S. *Electrochemical Methods: Fundamentals and Applications*; Wiley, 2022.
(60) Heller, I.; Kong, J.; Heering, H. A.; Williams, K. A.; Lemay, S. G.; Dekker, C. Individual Single-Walled Carbon Nanotubes as Nanoelectrodes for Electrochemistry. *Nano Lett.* **2005**, *5* (1), 137−142.
(61) Dominko, R.; Gaberšček, M.; Drofenik, J.; Bele, M.; Jamnik, J. Influence of carbon black distribution on performance of oxide cathodes for Li ion batteries. *Electrochim. Acta* **2003**, *48* (24), 3709−3716.
(62) Beverskog, B.; Puigdomenech, I. Revised pourbaix diagrams for iron at 25−300 °C. *Corros. Sci.* **1996**, *38* (12), 2121−2135.
(63) Komadel, P.; Madejová, J.; Janek, M.; Gates, W. P.; Kirkpatrick, R.; Stucki, J. W. Dissolution of hectorite in inorganic acids. *Clays Clay Miner.* **1996**, *44* (2), 228−236.
(64) Breen, C.; Madejová, J.; Komadel, P. Characterisation of moderately acid-treated, size-fractionated montmorillonites using IR and MAS NMR spectroscopy and thermal analysis. *J. Mater. Chem.* **1995**, *5* (3), 469−474.
(65) Tian-ming, G.; Fan, N.; Chen, W.; Dai, T. Lithium extraction from hard rock lithium ores (spodumene, lepidolite, zinnwaldite,

https://doi.org/10.1021/acs.est.5c11515
Environ. Sci. Technol. 2026, 60, 6162−6176

petalite): Technology, resources, environment and cost. *China Geology* **2023**, *6* (1), 137−153.
(66) Iyer, R.; Kelly, J. *Lithium Production in North America: A Review*, ANL/ESIA--23/8;185722; Argonne National Laboratory (ANL): Argonne, IL (United States): United States, 2023.
(67) Wesselkämper, J.; Hendrickson, T.; Smith, S.; Rao, P.; Haddad, A. Optimization of processing costs can make lithium extraction from clay competitive to conventional sources of brines and hard rock ores *ChemRxiv* DOI: 10.26434/chemrxiv-2025-ht4m3. (accessed January 1, 2026).
(68) Yang, L.; Yang, L.; Xu, G.; Feng, Q.; Li, Y.; Zhao, E.; Ma, J.; Fan, S.; Li, X. Separation and recovery of carbon powder in anodes from spent lithium-ion batteries to synthesize graphene. *Sci. Rep.* **2019**, *9* (1), No. 9823.
(69) Wolf, A.; Flegler, A.; Prieschl, J.; Stuebinger, T.; Witt, W.; Seiser, F.; Vinnay, T.; Sinn, T.; Gleiß, M.; Nirschl, H.; Mandel, K. Centrifugation based separation of lithium iron phosphate (LFP) and carbon black for lithium-ion battery recycling. *Chem. Eng. Process.—Process Intensif.* **2021**, *160*, No. 108310.
(70) Breen, C.; Madejová, J.; Komadel, P. Correlation of catalytic activity with infra-red, 29Si MAS NMR and acidity data for HCl-treated fine fractions of montmorillonites. *Appl. Clay Sci.* **1995**, *10* (3), 219−230.
(71) Komadel, P.; Janek, M.; Madejová, J.; Weekes, A.; Breen, C. Acidity and catalytic activity of mildly acid-treated Mg-rich montmorillonite and hectorite. *J. Chem. Soc., Faraday Trans.* **1997**, *93* (23), 4207−4210.
(72) Pálková, H.; Madejová, J.; Righi, D. Acid dissolution of reduced-charge Li-and Ni-montmorillonites. *Clays Clay Miner.* **2003**, *51* (2), 133−142.
(73) Rinaudo, C.; Roz, M.; Boero, V.; Franchini-Angela, M. FT-Raman spectroscopy on several di-and trioctahedral TOT phyllosilicates. *Neues Jahrb. Mineral., Monatsh.* **2004**, *2004*, 537−554.
(74) Moenke, H. H. W. Silica, the Three-Dimensional Silicates, Borosilicates and Beryllium Silicates. In *The Infrared Spectra of Minerals*; Farmer, V. C., Ed.; Mineralogical Society of Great Britain and Ireland, 1974; Vol. *4*.
(75) Craver, C. D.; Society, C. *The Coblentz Society Desk Book of Infrared Spectra*; The Society, 1982.
(76) MacKenzie, K. J. D.; Meinhold, R. H. The thermal reactions of synthetic hectorite studied by 29Si, 25Mg and 7Li magic angle spinning nuclear magnetic resonance. *Thermochim. Acta* **1994**, *232* (1), 85−94.
(77) Luhmer, M.; d'Espinose, J. B.; Hommel, H.; Legrand, A. P. High-resolution 29Si solid-state NMR study of silicon functionality distribution on the surface of silicas. *Magn. Reson. Imaging* **1996**, *14* (7), 911−913.
(78) O'Shaughnessy, C. A. The Structure of Alkali Silicate Glasses and Melts: A Multi-spectroscopic Approach. Ph.D. Thesis, University of Toronto: Canada—Ontario, CA, 2019.
(79) Akuzum, B.; Agartan, L.; Locco, J.; Kumbur, E. C. Effects of particle dispersion and slurry preparation protocol on electrochemical performance of capacitive flowable electrodes. *J. Appl. Electrochem.* **2017**, *47* (3), 369−380.
(80) Massiot, D.; Fayon, F.; Capron, M.; King, I.; Le Calvé, S.; Alonso, B.; Durand, J.-O.; Bujoli, B.; Gan, Z.; Hoatson, G. Modelling one- and two-dimensional solid-state NMR spectra. *Magn. Reson. Chem.* **2002**, *40* (1), 70−76.